molar volumes[25] of the base network upon AgI addition; such increases in molar volumes also progressively lower the T_g of the alloyed glasses (Fig. 1c, Fig. 2c).

Determining the physics of transport in ionic glasses continues to be challenging. It is necessary to understand aspects of molecular structure in order to understand the details[24,26] of the conduction process. In this respect, the identification of the glass transition temperatures of AgI and Ag_2Se will also be helpful in understanding the phase separation of these additives in oxide glasses. □

Methods

Stoichiometric As_2Se_3, AgI and elemental Ge, Ag and Se (99.999% purity from Cerac, Inc.) were used as starting materials to synthesize the pseudobinary A_xB_{1-x} alloy glasses (see text). Details of glass synthesis are in our earlier[10] work, where we examined the role of Ag as an additive in Ge-Se base glasses. T_gs were measured using a model 2920 MDSC (T.A. Instruments, Inc.) at a scan rate of 3 °C min^{-1}, and modulation rate of 1 °C per 100 s.

Received 16 November 2000; accepted 20 February 2001.

1. Tubandt, C. & Lorenz, E. Molekularzustand und elektrisches Leitvermögen kristallisierter Salze. *Z. Phys. Chem.* **24,** 513–543 (1914).
2. Bradley, J. N. & Greene, P. D. Solids with high ionic conductivity in group I halide system. *Trans. Faraday Soc.* **63,** 424–430 (1967).
3. Minami, T., Imazawa, K. & Tanaka, M. Formation region and characterization of superionic conductivity glasses in the systems AgI-Ag_2O-M_xO_7. *J. Non-Cryst. Solids* **42,** 469–476 (1980).
4. Rousselot, C. *et al.* The origins of neutron scattering prepeaks and conductivity enhancement in AgI-containing glasses. *Solid State Ionics* **78,** 211–221 (1995).
5. Kincs, J. & Martin, S. W. Non-Arrhenius conductivity in glasses: mobility and conductivity saturation effects. *Phys. Rev. Lett.* **76,** 70–73 (1996).
6. Swenson, J., McGreevy, R. L., Börjesson, L., Wicks, J. D. & Howells, W. S. Intermediate-range structure of fast-ion-conductivity. *J. Phys. Condens. Matter* **8,** 3545–3552 (1996).
7. Angell, C. A. Mobile ions in amorphous solids. *Annu. Rev. Phys. Chem.* **43,** 693–717 (1992).
8. Boolchand, P. & Bresser, W. J. The structural origin of broken chemical order in $GeSe_2$ glass. *Phil. Mag. B* **80,** 1757–1772 (2000).
9. Phillips, J. C. Topology of covalent non-crystalline solids I: short range order in chalcogenide alloys. *J. Non-Cryst. Solids* **34,** 153–181 (1979).
10. Mitkova, M., Wang, Y. & Boolchand, P. Dual chemical role of Ag as an additive in chalcogenide glasses. *Phys. Rev. Lett.* **83,** 3848–3851 (1999).
11. Feng, X., Bresser, W. J. & Boolchand, P. Direct evidence for stiffness threshold in chalcogenide glasses. *Phys. Rev. Lett.* **78,** 4422–4425 (1997).
12. Georgiev, D. G., Boolchand, P. & Micoulaut, M. Rigidity transitions and molecular structure of As_xSe_{1-x} glasses. *Phys. Rev.* B **62,** R9228–R9232 (2000).
13. Slivka, V. Y., Vysochanskii, Y. M., Stefanovich, V. A., Gerasimenko, V. S. & Chepur, D. V. Features of the vibrational spectra of $AgAsS_2$. *Sov. Phys. Solid State* **24,** 392–398 (1982).
14. Kerner, R. & Micoulaut, M. On the glass transition temperature in covalent glasses. *J. Non-Cryst. Solids* **210,** 298–305 (1997).
15. Micoulaut, M. The slope equations: a universal relationship between local structure and glass transition temperature. *Eur. Phys. J. B* **1,** 277–294 (1998).
16. Zhang, M. & Boolchand, P. The central role of broken bond-bending constraints in promoting glass formation in the oxides. *Science* **266,** 1355–1357 (1994).
17. Barnes, A. C., Lague, B. S., Salmon, S. P. & Fischer, H. E. A determination of the structure of liquid Ag_2Se using neutron diffraction and isotopic substitution. *J. Phys. Condens. Matter.* **9,** 6159–6173 (1997).
18. Phillips, J. C. *Bonds and Bands in Semiconductors* 45 (Academic, New York, 1973).
19. Nield, V. M., Keen, D. A., Hayes, W. & McGreevy, R. L. Structure and fast-ion conduction in α-AgI. *Solid State Ionics* **66,** 247–258 (1993).
20. Thorpe, M. F., Jacobs, D. J., Chubynsky, M. V. & Phillips, J. C. Self-organization in network glasses. *J. Non-Cryst. Solids* **266–269,** 859–866 (2000).
21. Cramer, C., Price, D. L. & Saboungi, M. L. Structure of AgI/Ag_2SeO_4 fast-ion conducting glasses: neutron diffraction experiments. *J. Phys. Condens. Matter.* **10,** 6229–6242 (1998).
22. Shastry, M. C. R. & Rao, K. J. Physico-chemical investigation of fast ion conducting AgI-Ag_2SeO_4 glasses. *Proc. Ind. Acad. Sci.* **102,** 541–553 (1990).
23. Zallen, R. *The Physics of Amorphous Solids* 190 (Wiley & Sons, New York, 1998).
24. Bunde, A., Funke, K. & Ingram, M. D. Ionic glasses: History and challenges. *Solid State Ionics* **105,** 1–13 (1998).
25. Swenson, J. & Börjesson, L. Correlation between free volume and ionic conductivity in fast ion conducting glasses. *Phys. Rev. Lett* **7,** 3569–3572 (1996).
26. Roling, B., Happe, A., Funke, K. & Ingram, M. D. Carrier concentrations and relaxation spectroscopy: new information from scaling properties of conductivity spectra in ionically conducting glasses. *Phys. Rev. Lett.* **78,** 2160–2163 (1997).

Supplementary information is available on *Nature*'s World-Wide Web site (http://www.nature.com) or as paper copy from the London editorial office of *Nature*.

Acknowledgements

We thank D.H. McDaniel, M. Mitkova, D. Georgiev, B. Goodman and M. Micoulaut for discussions. This work was supported by the Solid State Physics Program of the National Science Foundation.

Correspondence and requests for materials should be addressed to P.B. (e-mail: punit.boolchand@uc.edu).

Absence of deep-water formation in the Labrador Sea during the last interglacial period

C. Hillaire-Marcel*, A. de Vernal*, G. Bilodeau* & A. J. Weaver†

** GEOTOP, Université du Québec à Montréal, CP 8888, Montreal, Quebec, H3C 3P8 Canada*

† School of Earth and Ocean Sciences, University of Victoria, PO Box 3055, British Colombia, V8W 3P6, Canada

The two main constituent water masses of the deep North Atlantic Ocean—North Atlantic Deep Water at the bottom and Labrador Sea Water at an intermediate level—are currently formed in the Nordic seas and the Labrador Sea, respectively[1]. The rate of formation of these two water masses tightly governs the strength of the global ocean circulation and the associated heat transport across the North Atlantic Ocean[2]. Numerical simulations have suggested a possible shut-down of Labrador Sea Water formation as a consequence of global warming[3]. Here we use micropalaeontological data and stable isotope measurements in both planktonic and benthic foraminifera from deep Labrador Sea cores to investigate the density structure of the water column during the last interglacial period, which was thought to be about 2 °C

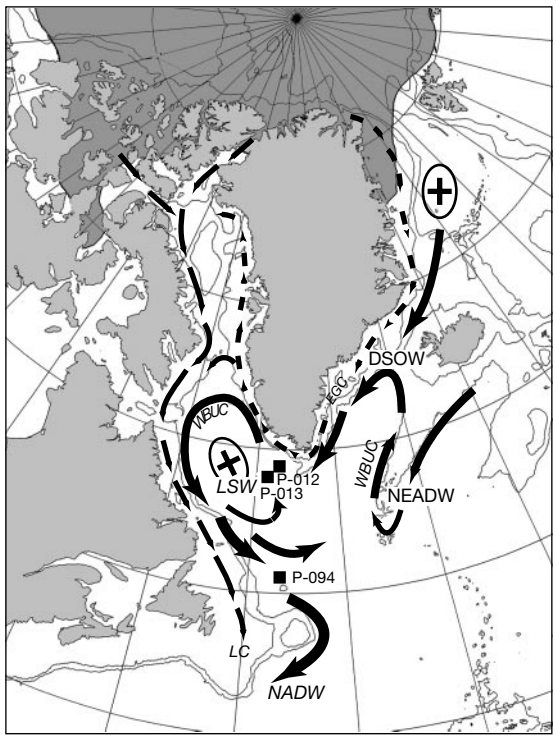

Figure 1 The Arctic–North Atlantic sector and the location of the study cores. Crosses: zones of formation of deep (DSOW) or intermediate (LSW) water. DSOW, Denmark Strait Overflow Water; LSW, Labrador Sea Water; NEADW, Northeast Atlantic Deep Water; NADW, North Atlantic Deep Water. Thin arrows, surface currents from the Fram Strait (dashed) and from the Arctic archipelago (continuous). EGC, East Greenland Current; LC, Labrador Current. Thick arrows, deep currents; WBUC, Western Boundary Undercurrent. The Arctic ice-pack (more than 11 months per year of sea-ice) is shown in dark grey. Coring sites were on the Greenland slope (P-012; 58° 55.35′ N, 47° 07.01′ W; 2,830 m), the Greenland rise (P-013; 58° 12.59′ N; 48° 22.40′ W; 3,380 m), and near Orphan knoll (P-094; 50° 12.26′ N, 45° 41.14′ W; 3,448 m).

warmer than present[4]. Our results indicate that today's stratification between Labrador Sea Water and North Atlantic Deep Water never developed during the last interglacial period. Instead, a buoyant surface layer was present above a single water mass originating from the Nordic seas. Thus the present situation, with an active site of intermediate-water formation in the Labrador Sea, which settled some 7,000 years ago, has no analogue throughout the last climate cycle.

The Nordic seas are separated from the North Atlantic by the Greenland–Scotland ridge, with a maximum depth of only about 600–800 m. Hence the renewal of the deep North Atlantic water is fed by an overflow of intermediate-depth water[5]. As these waters flow southwestwards in a deep western boundary current into the Labrador Sea, they entrain recirculating, relatively cold and fresh, Labrador Sea Water (LSW)[6,7] that is largely confined to the subpolar gyre of the North Atlantic[8] (Fig. 1). The deep western boundary undercurrent leaves the Labrador Sea at depths greater than ~2,000 m; this undercurrent is thought to be about 200–300 km wide, and to transport about 13–14 Sv of newly formed North Atlantic Deep Water (NADW)[9,10] southward before eventually encountering northward-flowing Antarctic Bottom Water. Despite the high salinity of the NADW, the colder Antarctic Bottom Water has higher density and passes below the NADW (see ref. 2 for a review).

The LSW mass is renewed locally through convective mixing during winter[1] (Fig. 2), although the amount of convection varies from year to year and from decade to decade (see, for example, Fig. 2 and refs 5, 6, 8, 11). Recent simulations conducted with the Hadley Centre coupled atmosphere–ocean model have suggested that over the next few decades, LSW mass formation could be practically stopped[3] as a consequence of global warming. Attempts at reconstructing the properties of LSW formation in geological episodes warmer than the present interglacial are thus needed to develop scenarios for changes induced by global warming, and to help in evaluating the projections of coupled models. The last interglacial—isotopic substage 5e (ISS-5e)[12]—constitutes an appropriate interval, as it experienced warmer conditions than the present. Although several studies suggest a high production rate of NADW during ISS-5e (see, for example, refs 13–15), the status of the Labrador Sea as a source of intermediate or upper North Atlantic deep water is still unclear. Here we address this issue, based on a reconstruction of past gradients of potential density (σ_θ) in the water column off southwestern Greenland (Fig. 1).

The reconstruction of conditions in the surface water layer rely on transfer functions based on organic-walled dinoflagellate cysts, or dinocysts, that provide estimates of salinities and temperatures for the warmest and coldest months, August and February[16]. Based on these estimates, we calculate values of σ_θ with a degree of accuracy ($\pm$0.4; see Fig. 3a and Methods) comparable to the interannual variability based on National Oceanographic Data Center (NODC) data sets. This interannual variability is clearly illustrated at the study site by the difference between profiles from the early 1990s, when enhanced production of LSW occurred[2], and the mean NODC values[17] of the preceding decades (Fig. 2).

We then reconstruct thermohaline conditions along the seasonal pycnocline between surface and underlying water masses from oxygen isotope compositions of foraminiferal calcite ($\delta^{18}O_c$) of epipelagic (*Globigerina bulloides*) and mesopelagic (*Neogloboquadrina pachyderma* left-coiling) planktonic taxa, following approaches illustrated in refs 18–21, whereas isotopic data from benthic foraminifers (*Cibicides wuellerstorfi*) provide complementary information on bottom water. The measured $\delta^{18}O_c$-values are converted into gradients of σ_θ using calibration equations derived from August and February temperatures and salinities in surface waters, assuming that they determine the seasonal range of σ_θ values (Figs 2d, 3b and Methods).

The study site is located slightly below the high-velocity core of the Western Boundary Under Current (WBUC) (core P-013; Fig. 1). This current—which at present winnows the lower slope where sedimentation rates are very low (see core P-012; Figs 1, 4a)—is responsible for sediment focusing in the deep basin. Periods with high production rate of Denmark Strait Overflow Water (DSOW), and thus high WBUC outflow, result in enhanced sedimentation rates on the rise and reduced rates on the slope (Fig. 4a, b). The Holocene and the last interglacial, associated here to ISS-5e, fall into this category, indicating high production rates of DSOW during the last interglacial as during the Holocene, in opposition to much lower production rates (when any) throughout the glacial interval.

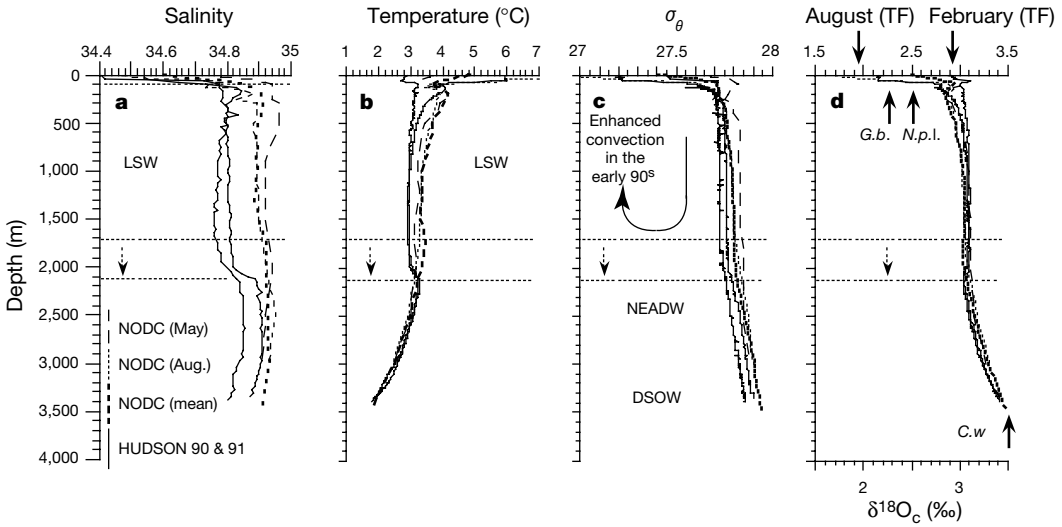

Figure 2 Structure of the modern water column at the Greenland rise site. **a**, Mean salinities from NODC data sets[17] versus 1990 and 1991 survey data on the CSS *Hudson*; **b**, mean temperatures from NODC data sets[17] versus 1990 and 1991 survey data; **c**, Potential-density values (σ_θ); **d**, Corresponding oxygen isotope composition ($\delta^{18}O_c$) for a calcite precipitated in isotopic equilibrium with ambient waters. The continuous arrows indicate $\delta^{18}O_c$ values for surface water conditions (respectively in August and February, based on transfer functions) and measured in foraminiferal assemblages from box-core sediments (*G.b.*, *Globigerina bulloides*; *N.p.*l.: *Neogloboquadrina pachyderma* left-coiling; *C.w.*, *Cibicides wuellerstorfi*). The dashed lines and arrows highlight the deepening of the pycnocline (dashed line) between the LSW and the NEADW in the early 1990s.

The inception of a modern-like situation during the early Holocene (Fig. 4c) is recorded through large isotopic offsets between the benthic foraminifers bathed by the DSOW, and planktonic foraminifers which develop along the pycnocline between the LSW and the surface layer. Transcribed into potential-density gradients, and compared with surface-water estimates (Fig. 4g), these values indicate the development of a LSW/NADW stratification early during the Holocene. However, it is only after ~7,000 ^{14}C yr BP that surface-water values of σ_θ in February exceed almost permanently those recorded by *Neogloboquadrina pachyderma* left-coiling, thus suggesting winter convection and production of LSW. Similar analyses performed on a core from the outlet of the NADW into the North Atlantic, at Orphan knoll (P-094; Fig. 1), indicate the same time frame for the development of a modern-like situation[18]. The two records also suggest maximum density values in surface waters, thus maximum LSW production, during the late Holocene (Fig. 4g). Both also depict large-amplitude, millennial-scale oscillations of density in surface waters, throughout the Holocene, that probably correspond to the pervasive millennial cycle described in the North Atlantic by Bond *et al.*[22]. These authors link these oscillations to ice-rafting events. Here, they seem driven by salinity changes (Fig. 4e).

The minima in salinity and density probably correspond to enhanced freshwater supplies from the Arctic into the Labrador Sea, possibly associated with reduced sea-ice cover in the Arctic[23]. Accordingly, maxima in salinity and density, with February σ_θ values in surface waters exceeding those values recorded by planktonic foraminifers (the black arrows in Fig. 4g), should reflect reduced freshwater supplies.

The freshwater export from the Arctic to the North Atlantic Ocean is governed by the total precipitation and runoff into the Arctic. Coupled modelling studies, such as that conducted by Wood *et al.*[3], suggest that a warmer world is one in which the hydrological cycle, and hence runoff into (and precipitation over) the Arctic, is enhanced. Freshwater export from the Arctic can either be in the form of sea ice or liquid water, and can leave the Arctic into the Atlantic through either the Fram Strait or the Canadian Archipelago. The freshwater export through the Fram Strait occurs via the narrow East Greenland Current which turns into the Labrador Sea at Cape Farewell as the West Greenland Current. Analogous to conditions which occurred in the late 1960s associated with the 'great salinity anomaly'[24], we can infer that when LSW formation was not in operation, as was the case during ISS-5e (see below), enhanced freshwater export from the Arctic probably occurred. Conversely, during intervals with enhanced LSW production, the net export of fresh water from the Arctic into the Labrador Sea was reduced.

The ISS-5e section at site P-013 indeed shows features very different from those of the Holocene, notably minimum isotopic offsets between planktonic and benthic foraminifers (Figs 4c, d). Here, ISS-5e can be subdivided into two climate episodes. As shown in Fig. 4d, a maximum abundance of *Osmunda* spores at ~121 kyr ago marks the transition between them. It indicates the spreading of a fern-rich vegetation over southern Greenland and spore transport through the riverine network[25]. The *Osmunda* maximum should thus match the maximum ice retreat over southern Greenland. The interval preceding the *Osmunda* maximum shows variable but generally low surface salinity conditions, and minimum values of σ_θ (Fig. 4d, f, h), probably due to high rates of ice meltwater supplies from the retreating ice-sheet. The late ISS-5e interval corresponds to more stable conditions in surface waters, with temperatures exceeding those of the Holocene (Fig. 4e, f). Throughout both intervals, σ_θ values in surface waters remained apparently too low to permit winter convection to occur (Fig. 4h). Even at the very end of ISS-5e (at ~117 kyr ago, Fig. 4h), when maximum σ_θ values are recorded in surface waters, σ_θ values in planktonic foraminifers still remained slightly higher.

As suggested by the very narrow bracket of σ_θ values between planktonic and benthic foraminifers (Fig. 4h) a single water mass seems to have occupied the water column below the low-density surface layer throughout the entire ISS-5e episode. Therefore, the Holocene-type LSW/NADW stratification never apparently developed during ISS-5e. The water mass then occupying the Labrador Sea, from its bottom up to very near its top, had a potential density slightly greater than that of the modern LSW. It ranged from 27.80 ± 0.16 (n = 168), at the level corresponding to the habitat of

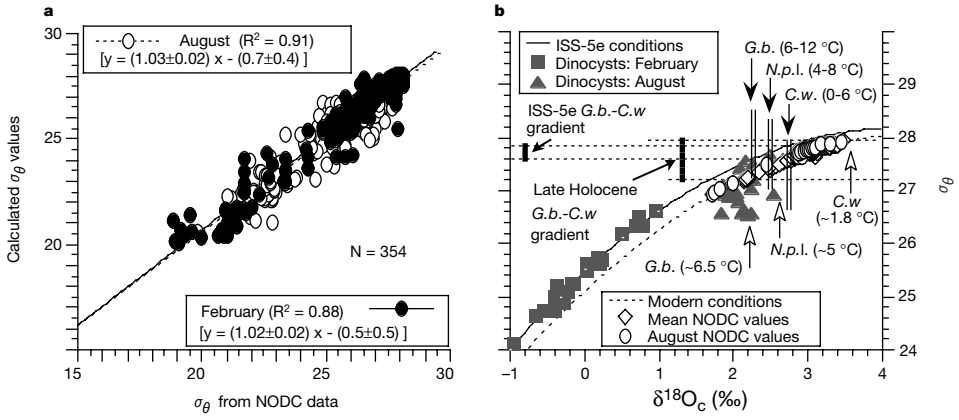

Figure 3 Estimation of potential-density values from proxies. **a**, Comparison of potential-density (σ_θ) estimates, using dinocyst assemblages from 354 core tops from the North Atlantic[16], with σ_θ values derived from NODC data sets at the corresponding sites. The strong correlation coefficients ($R^2 > 0.88$) provide an indication of the robustness of the σ_θ estimates. The scatter is due equally to variability in hydrographic measurements and to transfer-function uncertainty. The latter (that is, the standard deviation along the x axis) is ±0.4σ_θ units (±1 s.d.). **b**, Calibration of the relationship between values of σ_θ and $\delta^{18}O_c$ values in foraminiferal calcite. The equation for modern conditions is based on NODC data sets[17]: $\sigma_\theta = 25.1 + (1.3\delta^{18}O_c) - (0.14\delta^{18}O_c)^2$. The equation for ISS-5e is based on conditions in surface waters, from dinocyst transfer functions: $\sigma_\theta = 25.5 + (1.3\delta^{18}O_c) - (0.15\delta^{18}O_c)^2$. The ISS-5e equation has been constrained for high $\delta^{18}O_c$ values using maximum February σ_θ-values from transfer functions (grey triangles) and limits defined on the basis of ecological temperature ranges (the double vertical bars) of the foraminifer taxa used (the temperatures used to calculate the limits are shown in brackets). The difference between the Holocene and ISS-5e equations is essentially due to distinct boundary conditions (notably the difference of isotopic composition of fresh waters). Black arrows, mean $\delta^{18}O_c$ values of foraminiferal assemblages during ISS-5e; white arrows, mean $\delta^{18}O_c$ values during the Holocene (growth temperatures in brackets for each taxa are calculated from the projection of the measured $\delta^{18}O_c$ value on the calibration curve). Note the much narrower gradient of σ_θ values between *N.p.*l. and *C.w.* during ISS-5e compared with the Holocene.

Neogloboquadrina pachyderma left-coiling, to 27.90 ± 0.12 (n = 15), at the sea floor (Fig. 4h), and thus compares with that of the Holocene DSOW (27.94 ± 0.02; n = 18; Fig. 4g). This last interglacial water mass was probably produced in the Nordic seas. A high Denmark Strait overflow rate is indeed suggested by the strong WBUC outflow of the interval (Fig. 4a, b).

Although the Holocene and ISS-5e differ in many features, both interglacials depict the same large-amplitude, millennial-scale oscillations in surface-water σ_θ values. In both cases, salinity variations seem to be the determining factor (Fig. 4e,f). Oscillations in the Arctic ice-pack and related changes in freshwater outflow routes could be invoked for both intervals. Unfortunately, direct evidence for Arctic sea-ice conditions during the last interglacial that would support this hypothesis is still missing.

We can draw three conclusions from this study. (1) No LSW formation apparently occurred during the last interglacial, or during the subsequent ice age[18], and the modern-like LSW/NADW stratification never developed during the penultimate deglaciation. LSW formation, which became established mainly after 7,000 yr BP, seems to be a feature specific to the present interglacial. (2) Both the last and Holocene interglacials depict large-amplitude, millennial-scale oscillations in surface water density, possibly linked to sea-ice conditions in the Arctic and to the subsequent routing of fresh water into the North Atlantic. (3) The maximum ice retreat over Greenland, which followed an interval of low salinity and low density related to high meltwater supply rates, was in turn followed by the establishment of relatively warm winter conditions in the Labrador Sea.

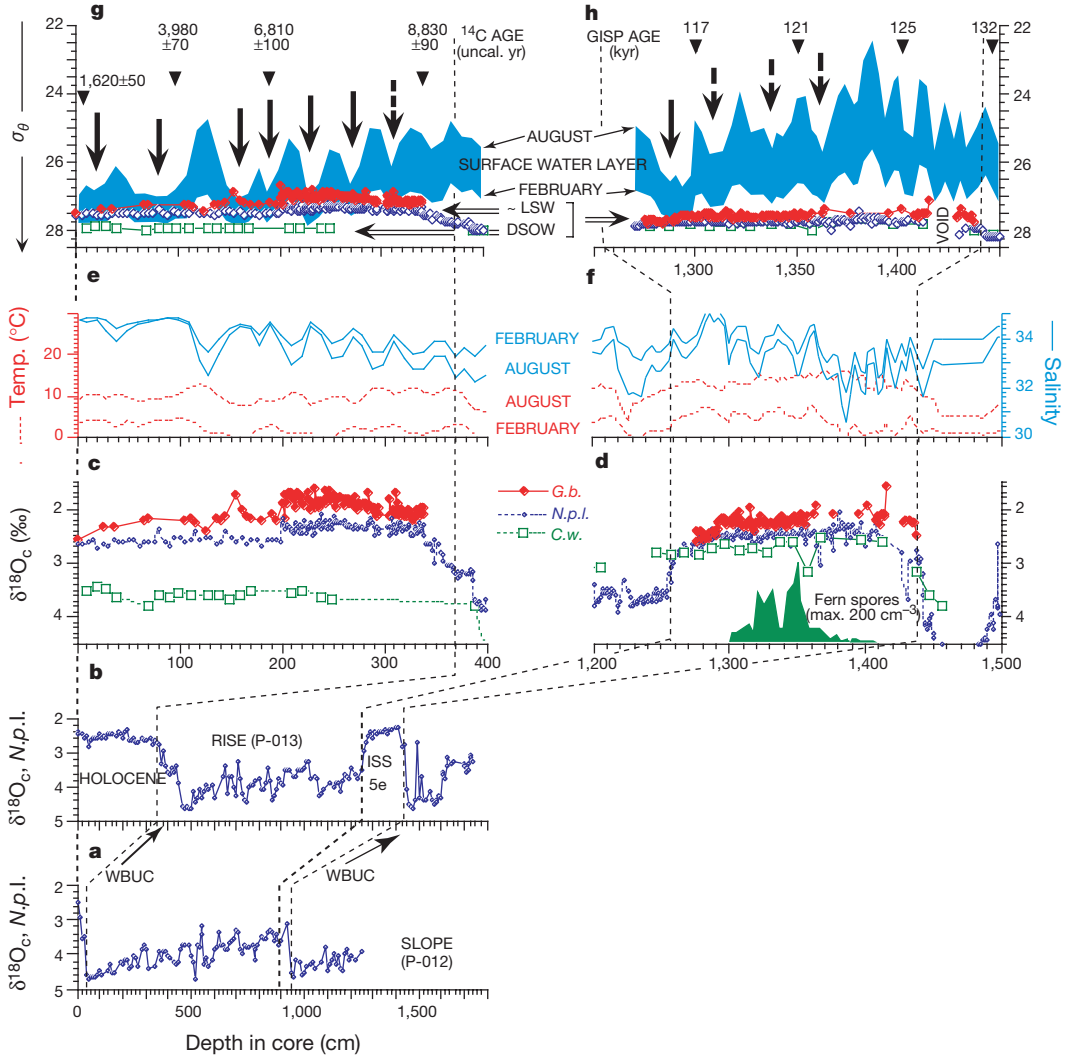

Figure 4 Magnified views of Holocene and ISS-5e records. **a** and **b**, Comparison of oxygen isotope stratigraphies at the emplacement of the high-velocity core of the WBUC (core P-012) and below it (core P-013), showing sediment focusing during interglacial intervals with high WBUC outflow (thus DSOW production)[29]. **c** and **d**, Oxygen isotope compositions ($\delta^{18}O_c$ values) of the epipelagic (*G.b.*), mesopelagic (*N.p.*l.) and benthic (*C.w.*) foraminifers during the Holocene and ISS-5e. $\delta^{18}O_c$ values in *C.w.* have been corrected by 0.64‰ for specific fractionation[26]. The fern-spore concentration curve of the ISS-5e section illustrates the maximum ice retreat over southern Greenland[25]. Complete data sets and references are available in ref. 29 and at http://www.unites.uqam.ca/geotop/ wwwgeotop.html. **e** and **f**, Temperature and salinity estimates (August versus February) from transfer functions for the Holocene and ISS-5e. **g** and **h**, Potential density gradients (reverse scale) in surface waters (grey area), from dinocyst transfer functions, and in underlying water masses, from $\delta^{18}O_c$ values in foraminifers. In **h**, the ISS-5e section is enlarged with respect to **d** and **f**. During ISS-5e, one single water mass seems to have occupied the whole water column below the dilute surface-water layer (no LSW formation, no LSW/NADW stratification). During the Holocene, notably after ~7,000 yr BP, winter σ_θ values in the surface exceed those of the underlying water mass suggested by *N.p.*l. data, indicating winter convection and LSW production. We note the large-amplitude, millennial-scale oscillations of salinity and density in surface waters during both interglacial intervals. The GISP-based chronology for the ISS-5e section is from Stoner *et al.*[30].

If we view the last interglacial, thought to be about 2 °C warmer than the present[4], as an analogue for a future climate warmed by anthropogenic greenhouse gases, we might expect the eventual permanent elimination of LSW formation, in accord with the model projection of Wood *et al.*[3]. We propose that the mechanism for the eventual shutdown would involve a move towards enhanced freshwater export from the Arctic into the Labrador Sea, as a consequence of an enhanced hydrological cycle in a warmer mean climate. □

Methods

Isotopic approaches

Oxygen isotope compositions of foraminiferal calcite was determined for specimens in the 150–250 and >150 μm size fractions, respectively, for planktics and benthics, and expressed in $\delta^{18}O$ values against the PDB standard (henceforth $\delta^{18}O_c$, in ‰, with $\delta^{18}O_c = [(^{18}O/^{16}O)_{sample}/(^{18}O/^{16}O)_{standard}] - 1$). Transcription of temperatures and salinities into $\delta^{18}O_c$ values is made through the equation:

$$t = (16.9 - 4.38)(\delta^{18}O_c - A) + 0.10(\delta^{18}O_c - A)^2, \text{ with } A = (\delta^{18}O_w - 0.27)$$

where t (in °C) stands for temperature during calcite precipitation, $\delta^{18}O_c$ for the oxygen isotope composition of calcite (versus the PDB standard), and $\delta^{18}O_w$ for the oxygen isotope composition of the ambient water expressed against standard mean ocean water (SMOW)[26]. $\delta^{18}O_w$ is linked to salinity (S) through a mixing equation between a 'standard ocean' ($\delta^{18}O_{sw}$ and S_{sw}) and the local freshwater ($\delta^{18}O_{fw}$, $S \approx 0$) end-members:

$$\delta^{18}O_w \approx \delta^{18}O_{sw} - [(\delta^{18}O_{fw} - \delta^{18}O_{sw}) \times (S_w - S_{sw})/S_{sw}]$$

S_w stands for the salinity of ambient waters. $\delta^{18}O_{fw}$, $\delta^{18}O_{sw}$ and S_{sw} constitute boundary conditions that varied through time, in response to mass transfers between oceans and ice sheets, and to a lesser extent, to the meltwater release and dispersal patterns[18]. For the Holocene and ISS-5e, we used $\delta^{18}O_{sw}$ = 0‰ and S_{sw} = 35. The Holocene and modern $\delta^{18}O_{fw}$ (local) value was set to −17.8‰ (ref. 27) and the ISS-5e $\delta^{18}O_{fw}$ to −16.3‰, assuming a difference proportional to that observed in the isotopic composition of Greenland ice between the two interglacials[28].

Transfer-function estimates and the σ_θ versus $\delta^{18}O_c$ relationship

Transfer functions based on dinocysts permit the reconstruction of temperature and salinity in the photic zone (essentially, the upper mixed layer). Dinocysts are abundant in sediments from estuarine to open-ocean environments, and are thus suitable for reconstructing past conditions along continental margins of the sub-Arctic[16]. Validation exercises of transfer functions yielded the following degree of accuracy: ±1.6 °C and ±1.2 °C, for mean temperatures in August and February, respectively, and ± 0.7 salinity units in the 25–36 salinity domain[16]. Most reconstructed values fall within the range of interannual variability of the hydrographic parameters. Salinity and temperature estimates are then used to calculate σ_θ values and compared with values from NODC data[17] (Fig. 3a). The scatter of σ_θ values around the $y = x$ line has a normal distribution with a standard deviation of ±0.54 (August + February data). As interannual variations of thermohaline conditions in surface waters are almost as large, uncertainties along the x axis of Fig. 3a ($\pm\sigma_x$, linked to transfer-function reconstructions) have been considered equivalent to those along the y axis (interannual variability), allowing us to retain a σ_x value of $(0.54 \times 2^{0.5}) \approx \pm 0.40$.

The seasonal and bathymetric ranges for the development of the planktic foraminifer taxa vary depending the hydrographic settings. In the Labrador Sea, where a strong seasonal pycnocline is observed, *Globigerina bulloides* develops during warmest months only (essentially, August) towards the top of the seasonal pycnocline, in shallow and relatively low density water, whereas *Neogloboquadrina pachyderma* left-coiling develops much earlier, since May, in colder, denser and deeper waters, that is, deeper along the seasonal pycnocline (see a review in ref. 18). Accordingly, *Globigerina bulloides* shows lower $\delta^{18}O_c$ values than *Neogloboquadrina pachyderma* left-coiling, and their isotopic compositions can thus be used to estimate density gradients along the seasonal pycnocline between the surface and the sub-surface water layers[18–21]. Here, a polynomial $\delta^{18}O_c$–σ_θ relationship is calibrated from hydrographic conditions in August and February (usually the warmest and coldest months, respectively), either using NODC hydrographic data sets (modern conditions) or estimates from dinocyst transfer functions (past or modern conditions). As shown in Fig. 2d, $\delta^{18}O_c$ estimates for February and August based on transfer functions encompass isotopic compositions measured for *Globigerina bulloides* and *Neogloboquadrina pachyderma* left-coiling. The $\delta^{18}O_c$–σ_θ calibration equation, based on such estimates, thus seems suitable for interpolating σ_θ values from measurements of $\delta^{18}O_c$ in planktonic foraminifers (Fig. 3b). It has also been used for benthic foraminifers. However, because $\delta^{18}O_c$ values in benthic foraminifers fall slightly outside the range defined for surface waters (Fig. 3b), and because bottom-water masses may have different ages and hydrographic histories from surface waters, the corresponding σ_θ values are possibly less accurate.

Statistical assessment of past σ_θ values

Reconstructions of mean σ_θ values for ISS-5e and the past 7 kyr (the period of the Holocene with LWS formation) are based on 41, and 18 or more, data points, respectively. The corresponding mean σ_θ estimates for surface waters in February are of 26.72 ± 0.43 (n = 41) and 27.56 ± 0.26 (n = 18), respectively. Those calculated for the subsurface water layer, based on data from *Neogloboquadrina pachyderma* left-coiling, are 27.80 ± 0.16 (n = 168) and 27.51 ± 0.05 (n = 34), respectively. At >95% confidence interval, these values indicate density gradients compatible with winter convection, during the interval from 7 kyr ago to the present, but much too strong during ISS-5e for such deep mixing to have occurred.

Received 9 October 2000; accepted 23 February 2001.

1. Marshall, J. & Schott, F. Open-ocean convection; observations, theory, and models. *Rev. Geophys.* **37,** 1–64 (1999).
2. Weaver, A. J., Bitz, C. M., Fanning, A. M. & Holland, M. Thermohaline circulation: High latitude phenomena and the difference between the Pacific and Atlantic. *Annu. Rev. Earth Planet. Sci.* **27,** 231–285 (1999).
3. Wood, R. A., Keen, A. B., Mitchell, J. F. B. & Gregory, J. M. Changing spatial structure of the thermohaline circulation in response to atmospheric CO_2 forcing in a climate model. *Nature* **399,** 572–575 (1999).
4. White, J. W. C. Don't touch that dial. *Nature* **364,** 186 (1993)
5. Aagaard, K., Swift, J. H. & Carmack, E. C. Thermohaline circulation in the Arctic Mediterranean seas. *J. Geophys. Res.* **90,** 4833–4846 (1985).
6. Dickson, R. R. & Brown, J. The production of North Atlantic deep water: Sources, sinks and pathways. *J. Geophys. Res.* **99,** 12319–12341 (1994).
7. McCartney, M. S. Recirculating components to the deep boundary current of the northern North Atlantic. *Prog. Oceanogr.* **29,** 283–383 (1992).
8. McCartney, M. S. & Talley, L. D. Warm-to-cold water conversion in the northern North Atlantic Ocean. *J. Phys. Oceanogr.* **14,** 922–935 (1984).
9. Schmitz, W. J. Jr & McCartney, M. S. On the North Atlantic circulation. *Rev. Geophys.* **31,** 29–49 (1993).
10. Talley, L. D. & McCartney, M. S. Distribution and circulation of Labrador Sea Water. *J. Phys. Oceanogr.* **12,** 1189–1205 (1982).
11. Dickson, R. R., Lazier, J., Meincke, J., Rhines, P. & Swift, J. Long-term coordinated changes in the convective activity of the North Atlantic. *Prog. Oceanogr.* **38,** 205–239 (1996).
12. Shackleton, N. J. Oxygen isotopes, ice volume and sea level. *Quat. Sci. Rev.* **6,** 183–190 (1987).
13. Yu, E. F., Francois, R. & Bacon, M. P. Similar rates of modern and last-glacial ocean thermohaline circulation inferred from radiochemical data. *Nature* **379,** 689–694 (1996).
14. Keigwin, L. D., Curry, W. B., Lehman, S. J. & Johnsen, S. The role of the deep ocean in North Atlantic climate change between 70 and 130 kyr ago. *Nature* **371,** 323–326 (1994).
15. Adkins, J. F., Boyle, E. A., Keigwin, L. & Cortijo, E. Variability of the North Atlantic thermohaline circulation during the last interglacial period. *Nature* **390,** 154–156 (1997).
16. de Vernal, A., Rochon, A., Turon, J.-L. & Matthiessen, J. Organic-walled dinoflagellate cysts: palynological tracers of sea-surface conditions in middle to high latitude marine environments. *Geobios* **30,** 905–920 (1997).
17. National Oceanographic Data Center *World Ocean Atlas* CR-ROM (National Oceanic and Atmospheric Administration, Boulder, 1994).
18. Hillaire-Marcel, C., de Vernal, A., Bilodeau, G. & Stoner, J. Changes of potential density gradients in the northwestern North Atlantic during the last climatic cycle based on a multiproxy approach. *Am. Geophys. Union. Monogr.* (in the press).
19. Kohfeld, K. E., Fairbanks, R. G., Smith, S. L. & Walsh, I. D. *Neogloboquadrina pachyderma* (sinistral coiling) as paleoceanographic tracers in polar oceans: Evidence from Northeast Water Polynya plankton tows, sediment traps, and surface sediment. *Paleoceanography* **11,** 679–699 (1996).
20. Andreasen, D. J & Ravelo, A. Tropical Pacific Ocean thermocline depth reconstruction for the last glacial maximum. *Paleoceanography* **2,** 395–413 (1997).
21. Faul, K., Ravelo, A. C. & Delanay, M. L. Reconstructions of upwelling, productivity, and photic zone depth in the eastern equatorial Pacific ocean using planktonic foraminiferal stable isotopes and abundances. *J. Foram. Res.* **30,** 110–125 (2000).
22. Bond, G. *et al.* Pervasive millennial-scale cycle in the North Atlantic Holocene and glacial climate. *Science* **278,** 1257–1266 (1997).
23. de Vernal, A. *et al.* Sea-ice cover and sea surface conditions in the Arctic and circum-Arctic during the Holocene: Preliminary results and methodological issues. *Can. Geophys. Union Mtg* (abstr.) (2000).
24. Dickson, R. R., Meincke, J., Malmberg, S. A. & Lee, A. J. The "great salinity anomaly" in the Northern North Atlantic 1968–1982. *Prog. Oceanogr.* **20,** 103–151 (1988).
25. de Vernal, A., Miller, G. & Hillaire-Marcel, C. Paleoenvironments of the last interglacial sensu lato in northwest North Atlantic regions: eastern Canada and adjacent seas. *Quat Int.* **10-12,** 95–106 (1991).
26. Shackleton, N. J. in *Méthodes Quantitatives d'étude des Variations du Climat au Cours du Pléistocène* (ed. Labeyrie, J.) 203–209 (Editions du CNRS, Paris, 1974).
27. Wu, G.-P. & Hillaire-Marcel, C. Oxygen isotope compositions of sinistral *Neogloboquadrina pachyderma* tests in surface sediments: North Atlantic Ocean. *Geochim. Cosmochim. Acta* **58,** 1303–1312 (1994).
28. Dansgaard, W. *et al.* Evidence for general instability of past climate from a 250-kyr ice-core record. *Nature* **364,** 218–220 (1993).
29. Hillaire-Marcel, C. (ed.). The Labrador Sea during the late Quaternary. *Can. J. Earth Sci. (Special issue)* **31** (1994).
30. Stoner, J. S., Channell, J. E. T. & Hillaire-Marcel, C. A 200 kyr geomagnetic stratigraphy for the Labrador Sea: Indirect correlation of the sediment record to SPECMAP. *Earth Planet. Sci. Lett.* **159,** 165–181 (1998).

Acknowledgements

This study is a contribution to the Climate System, History and Dynamics project, supported by the National Science and Engineering Research Council of Canada, and to the international Images program. Complementary support by the Fonds pour la Formation de chercheurs et l'Aide à la Recherche of Quebec Province is acknowledged.

Correspondence and requests for materials should be addressed to C.H.-M. (e-mail: chenv@uqam.ca).